JACS
JOURNAL OF THE AMERICAN CHEMICAL SOCIETY
pubs.acs.org/JACS
Article

High-Entropy Perovskite Oxide Enables Visible-Light-Driven Overall Water Splitting via "inner-Z-Scheme" Pathway

Hao Ling, Aomiao Zhi, Lei Liao, Yuanfang Feng, Yingying Lan, Lejuan Cai, Xudan Huang, Lisha Lu, Renjie Li, Qi Guo, Meiyun Li, Jingkun Zhang, Lifen Wang, Muhua Sun,* Xuedong Bai, and Wenlong Wang*

Cite This: J. Am. Chem. Soc. 2026, 148, 25696−25706
Read Online
ACCESS | Metrics & More | Article Recommendations | Supporting Information

ABSTRACT: The high degree of chemical complexity and expanded compositional space enabled by high-entropy engineering offers opportunities for rationally designing new type semiconductor photocatalysts with tailored electronic structure favorable for full-spectrum solar energy utilization. Here, we construct a high-entropy photocatalyst featuring an "inner-Z-scheme" stepwise photoexcitation that enables efficient visible-light-driven overall water splitting. This inner-Z-scheme is realized through the formation of a delocalized intermediate band within the wide bandgap of a perovskite $NaNbO_3$ host, achieved by selectively incorporating closed-shell d^0 and open-shell d^n transition-metal cations into a single-phase solid solution. Electron microscopy confirms that the resulting high-entropy perovskite oxide (termed $Na(HE)O_3$) retains a highly crystalline structure while exhibiting the short-range lattice distortions characteristic of high-entropy materials. Complementary spectroscopic analyses identify a pronounced intermediate-band feature that enables sequential sub-bandgap electronic excitation and extends the photoresponse into the visible region. The compositional diversity further creates varied local coordination environments with the formation of intrinsic catalytic centers to enable overall water splitting without additional cocatalysts. Under AM 1.5G solar illumination, $Na(HE)O_3$ achieves stable overall water splitting with a solar-to-hydrogen efficiency of 1.34%. This work establishes high-entropy-stabilized intermediate-band semiconductors as a viable platform for band-structure engineering in photocatalyst design.

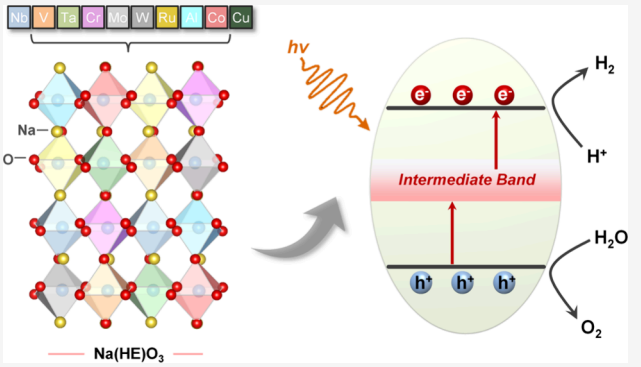

INTRODUCTION

Solar-driven photocatalytic water splitting is an important pathway toward sustainable hydrogen production.[1,2] In this context, direct overall water splitting by photocatalysis without the use of sacrificial agents or external bias is particularly appealing because it relies on the simplest reaction scheme that is suitable for large-scale implementation.[3,4] Although some wide bandgap semiconductors have enabled this reaction under ultraviolet illumination, extending the overall water splitting to the visible-light region remains difficult.[5,6] The key challenge is that a single semiconductor must simultaneously straddle the redox potentials required for both hydrogen and oxygen evolution while also possessing a sufficiently narrow bandgap to absorb low-energy visible photons.[7−10] Alternatively, another effective strategy is to couple two complementary semiconductors to construct Z-scheme or S-scheme heterojunctions, in which two-step excitation allows the utilization of low-energy light for overall water splitting.[11−15] In principle, such two-step visible-light excitation does not have to rely on a "two-component" system but could instead be realized within a single semiconductor. If a suitably positioned intermediate band can be incorporated within the wide band-gap of a semiconductor, a conceptually different "inner-Z-scheme" two-step photoexcitation pathway will be established in a Z-scheme-like manner, through which electrons accumulate energy via stepwise transitions mediated by intermediate band. In previous studies of intermediate-band solar cells, initial evidence for the feasibility of intermediate-band-mediated photon harvesting has been demonstrated.[16−18] However, practical materials capable of supporting an inner-Z-scheme that can be exploited for photocatalysis remain extremely scarce. In pursuit of breakthrough innovations, the emerging concept of high-entropy semiconductors may offer a unique opportunity to overcome this material bottleneck.

Received: February 7, 2026
Revised: May 29, 2026
Accepted: June 1, 2026
Published: June 17, 2026

https://doi.org/10.1021/jacs.6c02884
J. Am. Chem. Soc. 2026, 148, 25696−25706

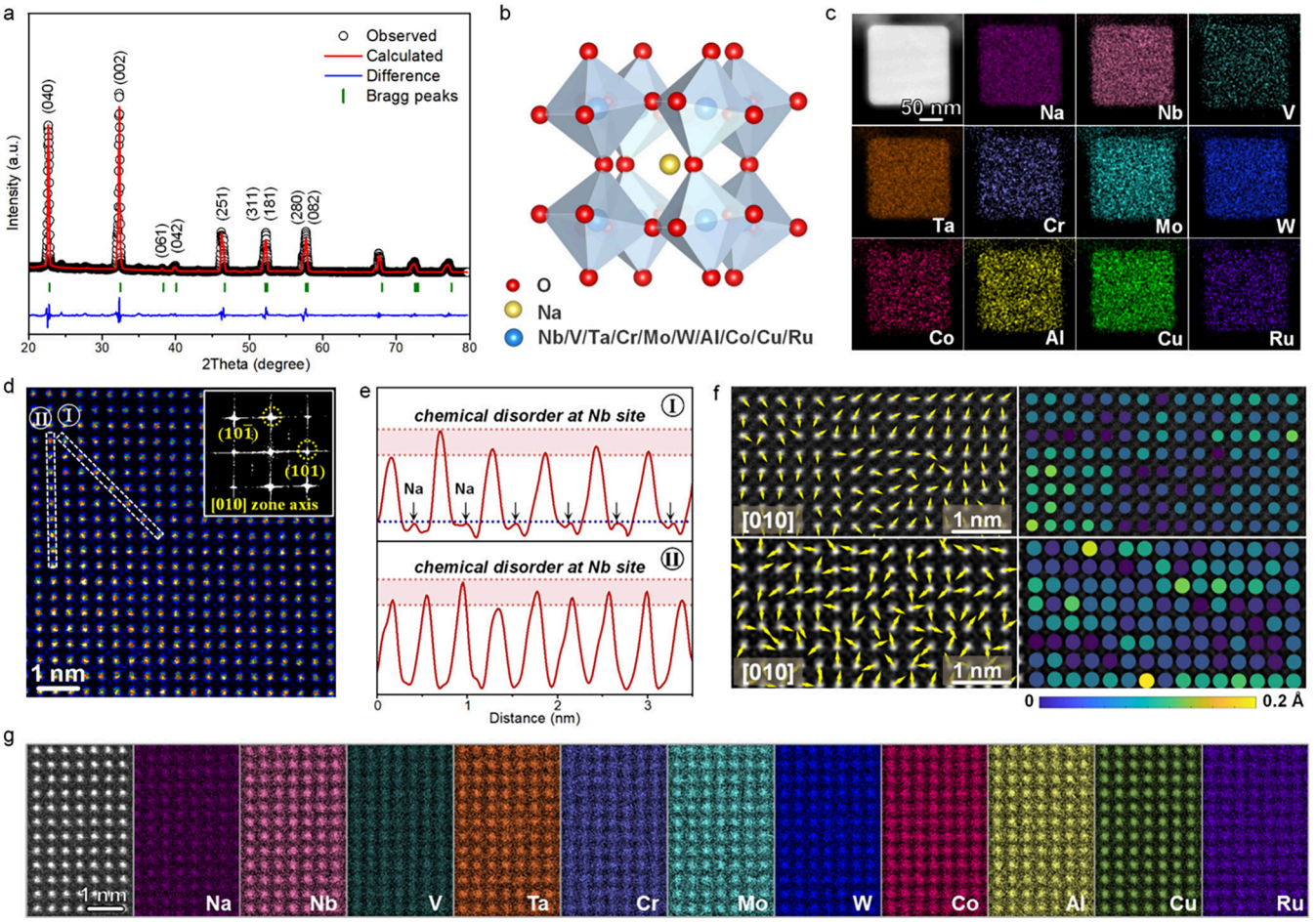

Figure 1. Microstructural and elemental characterization of $Na(HE)O_3$ sample. (a) XRD pattern together with related Rietveld refinement result. (b) Schematic illustration of the perovskite crystal structure of $Na(HE)O_3$, where Na occupies the A sites and high-entropy metal cations occupy the B sites. (c) EDS elemental mapping of a single $Na(HE)O_3$ nanocube. (d) Atomic-resolution HAADF-STEM images along the [010] zone axis, where bright spots correspond to B-site metal cations columns. Inset: the corresponding FFT pattern. (e) HAADF intensity profiles showing the variation of intensities of cation column rows from the white line I and line II in (d). (f) Maps of the magnitude and direction of cation displacements, illustrating local lattice distortion in the different areas of the high-entropy lattice, projected along the [010] zone axes. (g) Atomic-resolution STEM-EDS elemental mapping of a randomly selected interior region of the particle, further confirming the coexistence of all metal elements at the B sites within the perovskite framework.

High-entropy materials incorporate multiple elements into a single-phase solid solution that possess significant configurational entropy.[19,20] Their vast compositional space and the associated significant chemical complexity offer a versatile platform for designing efficient catalytic materials, including photocatalyst.[21−23] First, the coexistence of diverse local chemical environments naturally generates a broad distribution of coordination geometries, producing an almost continuous spectrum of adsorption energies at catalytic sites—a feature rarely realized in conventional photocatalytic systems.[24−28] Photocatalysis represents a special form of heterogeneous catalysis. Besides the issue of catalytic sites engineering, the sufficiently strong light absorption is also an essential prerequisite in photocatalysis.[29] From a band-structure perspective, high-entropy oxide semiconductors hold great promise for achieving enhanced light harvesting via two principal mechanisms.[30,31] One arises from band broadening at the valence-band maximum and conduction-band minimum due to extensive d-orbital hybridization among multiple metal cations, leading to bandgap narrowing.[32−35] The other involves the formation of delocalized intermediate bands within a wide bandgap through appreciated orbital overlap, which underpins the stepwise excitation pathway required for an inner-Z-scheme.

In conventional low-entropy wide bandgap oxide semiconductors (e.g., TiO_2), electronic structure engineering via substitutional doping with alien transition-metal cations is widely used to achieve visible-light absorption.[36−39] However, such doping typically introduces discrete impurity states that act as nonradiative recombination centers, severely limiting carrier lifetimes. In contrast, high-entropy stabilized metal oxides formed by strategic incorporation of multiple transition-metal cations can fundamentally alter this scenario.[35,40−42] Instead of isolated trap states, strong electronic coupling among multiple d-orbital manifolds produces a delocalized, quasi-continuous intermediate band with substantial energy dispersion. This feature will effectively suppress nonradiative recombination and enable nearly unimpeded carrier migration. In addition, the intermediate band can also function as an electronic "relay" to support efficient two-step excitation, thereby constituting an inner-Z-scheme excitation process for harvesting the low-energy photons.[17] Along this line, a viable strategy to construct a practical inner-Z-scheme light-harvesting framework is the rational combination of closed-shell d^0/

https://doi.org/10.1021/jacs.6c02884
J. Am. Chem. Soc. 2026, 148, 25696−25706

d^{10} cations with open-shell d^n transition-metal cations within a single-phase solid solution of high-entropy oxides, where the d^0/d^{10} cations define a widely gaped band matrix and the open-shell d^n cations will lead to the formation of the intermediate band.[43,44]

Here in this work, we present the first demonstration of such a design concept by using wide-bandgap perovskite $NaNbO_3$ as the host lattice for high-entropy engineering. Multiple transition-metal cations, including closed-shell d^0 cations (Nb^{5+}, Ta^{5+}) and open-shell cations (V^{4+}, Cr^{3+}, Mo^{5+}, W^{5+}, Ru^{4+}, Co^{2+}, Cu^{2+}), are incorporated into the $NaNbO_3$ lattice to form a high-entropy perovskite oxide denoted as $Na(HE)O_3$. All of these cations randomly and uniformly occupy the Nb sublattice, accompanied by short-range lattice distortions characteristic of high-entropy structures. Moreover, because of local charge-compensation effects within the high-entropy lattice, together with the presence of oxygen vacancies, these constituent elements tend to exhibit mixed oxidation states. We show that $Na(HE)O_3$ undergoes substantial reconstruction of its electronic band structure relative to pristine $NaNbO_3$, featuring an extended intermediate band derived primarily from open-shell cations and positioned between the widely separated valence and conduction bands defined by closed-shell d^0 cations. This intermediate band enables a Z-scheme-like two-step excitation process, leading to broad-spectrum absorption with strong overlap with the solar spectrum and prolonged carrier lifetimes favorable for photocatalysis. Importantly, the open-shell transition-metal cations introduced for intermediate-band regulation, such as Ru and Co, also function as built-in surface catalytic sites for activating water redox reactions. The nontrivial combination of efficient light harvesting and naturally occurring catalytic sites within a single material enables visible-light-driven overall water splitting without additional cocatalysts, a capability achieved by only a limited number of photocatalytic systems.

RESULTS AND DISCUSSION

The $Na(HE)O_3$ nanocubes were synthesized via a controlled two-step molten-salt method using a mixed NaCl-KCl molten-salt system. In this system, NaCl served as the Na source as well as the flux, while KCl served as a secondary flux to lower the melting temperature.[45] This binary molten-salt medium facilitated efficient mass transport, enabling the deliberate incorporation of ten metal cations (Nb/V/Ta/Cr/Mo/W/Co Al/Cu/Ru) into the Nb sites, namely, the B sites of the ABO_3 perovskite lattice of $NaNbO_3$. As shown in Figures 1a and S1, the X-ray diffraction (XRD) pattern of $Na(HE)O_3$ matches well with that of pristine $NaNbO_3$, with no detectable secondary impurity phases. Rietveld refinement also confirms that $Na(HE)O_3$ nanocubes crystallize as a single-phase perovskite with space group *Pbcm* (Figure 1b). Moreover, the refined lattice parameters (a = 5.58 Å, b = 15.63 Å, and c = 5.53 Å) are slightly larger than those of pristine $NaNbO_3$, arising from the coexistence of multiple B-site cations with different ionic radii (Figure S2 and Table S1). Elemental stoichiometries were quantified by inductively coupled plasma-atomic emission spectroscopy (ICP-AES). There are minor deviations from the nominal precursor ratios observed, which can be attributed to the distinct dissolution behaviors of different transition-metal ions in the molten-salt medium (Table S2). Based on the measured compositions, the configurational entropy of $Na(HE)O_3$ was calculated to be ~1.81R for the B-site cation sublattice and 1.09R per mole of atoms across all sublattices, thereby confirming the high-entropy stabilization of this single-phase $Na(HE)O_3$ structure.[46,47]

The morphology of $Na(HE)O_3$ was characterized by scanning electron microscopy (SEM), revealing that the sample are uniform nanocubes with an average size of ~80 nm (Figure S3). Besides, energy-dispersive X-ray spectroscopy (EDS) mapping acquired in the aberration-corrected scanning transmission electron microscopy (STEM) mode (Figure 1c) shows that all constituent elements, including Na and the B-site metal cations (Nb/V/Ta/Cr/Mo/W/Co/Al/Cu/Ru), are homogeneously distributed within an individual $Na(HE)O_3$ nanocube. To further elucidate the local atomic structure, high angle annular dark field (HAADF) and annular bright field (ABF) imaging were performed using aberration-corrected STEM. As shown in Figure 1d, the HAADF image acquired along the [010] zone axis exhibits a well-resolved periodic lattice, where the bright columns correspond to metal cations occupying the perovskite B sites. The corresponding fast Fourier transform (FFT) pattern in the inset exhibits distinct diffraction spots with slight diffuseness, suggesting that the long-range ordering is well preserved despite great chemical complexity. Moreover, multiple $Na(HE)O_3$ nanocubes were systematically examined using aberration-corrected HAADF-STEM. Particular attention was paid to different local regions within individual particles, especially edge and near-surface areas, to evaluate possible local structural variations. The results show that all nanocubes, as well as their distinct local regions, exhibit continuous and well-defined lattice fringes, with no observable amorphous domains or secondary phase features (Figure S4). These characterization techniques collectively provide consistent evidence across multiple length scales, highlighting the structural uniformity and robust crystallinity characteristics of the $Na(HE)O_3$ samples.

In addition, adjacent bright atomic columns in these HAADF images exhibit obvious contrast variations arising from Z-contrast differences among the different metal cations occupying the B sites. As presented in Figure 1e, taking the [010] zone axis as an example, the HAADF intensity profiles are extracted along two representative line scans (lines I and II, marked by the white lines in Figure 1d). Line I, passing through adjacent B-site atomic columns, shows pronounced intensity fluctuations that originate from the random occupancy of these metal cations with different atomic numbers. On the other hand, line II likewise reveals strong contrast variations at the B sites, together with weaker intensity features between adjacent metal columns, which are attributed to the Na atomic layers. These observations confirm that chemical disorder is confined to the B-site sublattice, whereas Na cations stably occupy the A-site sublattice.

Such chemical complexity within the high-entropy lattice is often associated with local lattice distortions.[48] This could be visualized by the displacement magnitude and direction maps of B-site cations projected along the [010] zone axes (Figure 1f). The results reveal nonuniform atomic displacements with a maximum magnitude of approximately 0.2 Å, indicative of local lattice distortion characteristic of high-entropy oxides. Moreover, the atomic-resolution STEM-EDS mapping also confirms the coexistence of all ten kinds of metal elements at the B sites, while just Na occupies the A sites, with all elements following the periodic perovskite framework (Figure 1g). Collectively, these results demonstrate that $Na(HE)O_3$ simultaneously preserves long-range crystallographic order while exhibiting

https://doi.org/10.1021/jacs.6c02884
J. Am. Chem. Soc. 2026, 148, 25696−25706

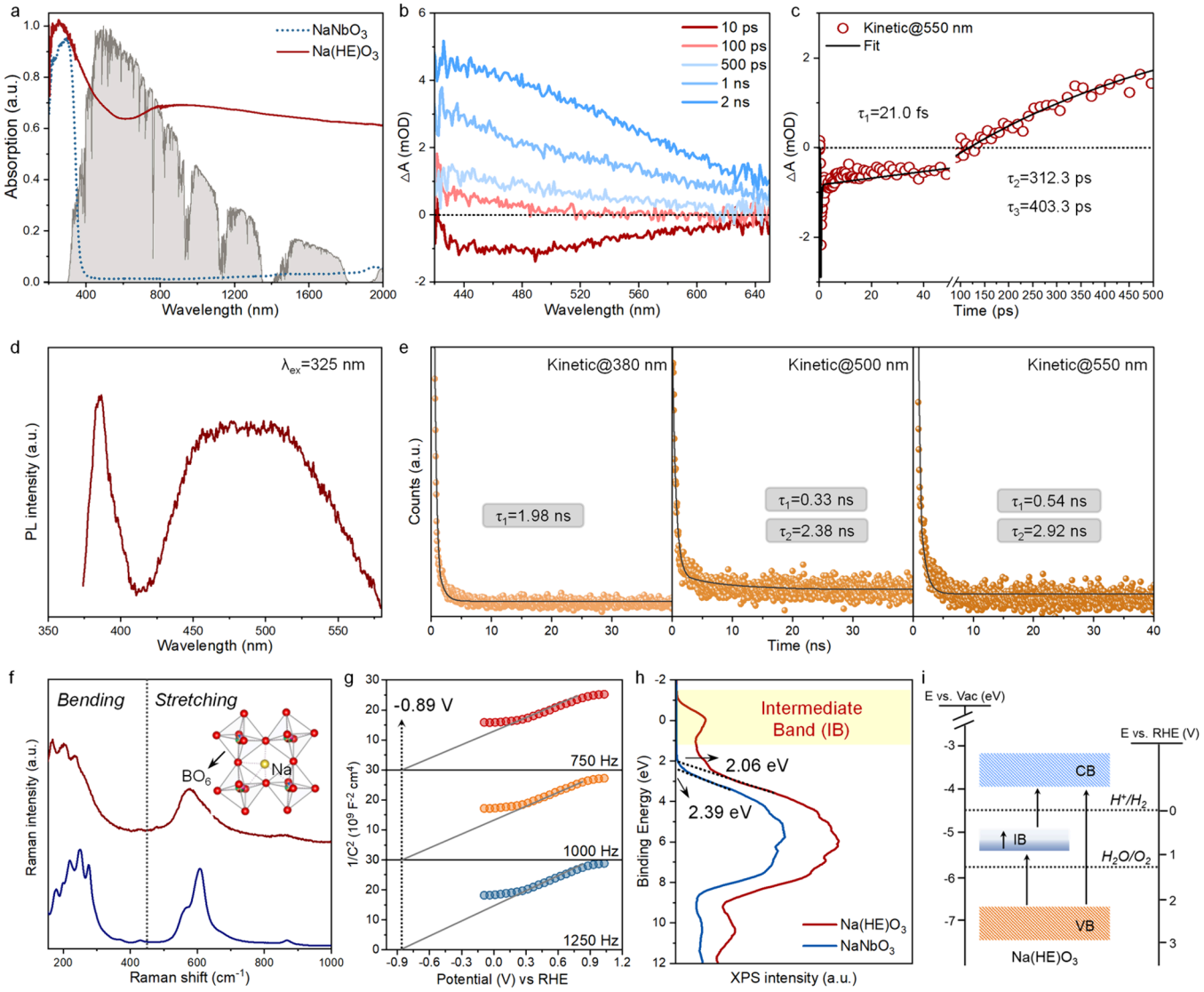

Figure 2. Optical performance and photocarrier dynamic analysis of $Na(HE)O_3$ sample. (a) Diffuse reflectance UV−vis spectra of the $Na(HE)O_3$. (b) Transient absorption spectra at various time delays of $Na(HE)O_3$ after pumping at 365 nm. (c) Corresponding decay kinetics probed at 550 nm. (d) Photoluminescence spectra of $Na(HE)O_3$ excited at 325 nm, indicating multiple possible radiative recombination pathways. (e) Representative time-resolved photoluminescence decay curves of the band-edge emission at 380 nm and visible emissions at 500 and 550 nm. (f) Raman spectra of $Na(HE)O_3$ and pristine $NaNbO_3$. The inset shows a schematic illustration of the BO_6 octahedron in $NaNbO_3$. (g) Mott−Schottky plots of $Na(HE)O_3$ measured at different frequencies. (h) Valence band XPS spectra of $Na(HE)O_3$ and pristine $NaNbO_3$. The shaded yellow regions denote intermediate-band states formed within the high-entropy lattice. (i) Schematic band structure diagram of as-synthesized $Na(HE)O_3$, illustrating band-edge positions and intermediate band formation induced by the incorporation of mixed closed-shell and open-shell cations at B sites.

local structural disorder with diverse bonding environments. This combination not only is a defining structural feature arising from the high-entropy effect in $Na(HE)O_3$ but also provides the structural basis for electronic-structure modulation.

Fundamentally, the electronic structure of transition-metal oxides is intimately coupled to their structural configurations. For example, lattice parameters, which define atomic spacing and long-range crystalline periodicity, directly modulate electron delocalization and bandwidth, while the local coordination environment governs the hybridization between metal centers and surrounding oxygen atoms, thereby influencing d-orbital splitting and charge distribution.[49] High-entropy oxides, in particular, combine long-range lattice order with diverse local coordination environments around individual metal cations. This unique structural feature enables broad redistribution of electronic states rather than isolated defect levels.[40,50,51] This electronic reconstruction is reflected in the optical properties. As shown in Figure 2a, although $Na(HE)O_3$ crystallizes in a perovskite structure similar to pristine $NaNbO_3$, their optical properties are apparently different. The diffuse reflectance UV−vis spectrum of $Na(HE)O_3$ shows continuous broadband absorption extending from the UV to the near-infrared region, together with a pronounced absorption band centered at approximately 800 nm. Such changes in the optical response can be reasonably ascribed to a substantial reconfiguration of the electronic band structure, which involves not only band-edge modulation but also the emergence of mid-gap electronic states. To study the corresponding photogenerated carrier dynamics, transient

https://doi.org/10.1021/jacs.6c02884
J. Am. Chem. Soc. 2026, 148, 25696−25706

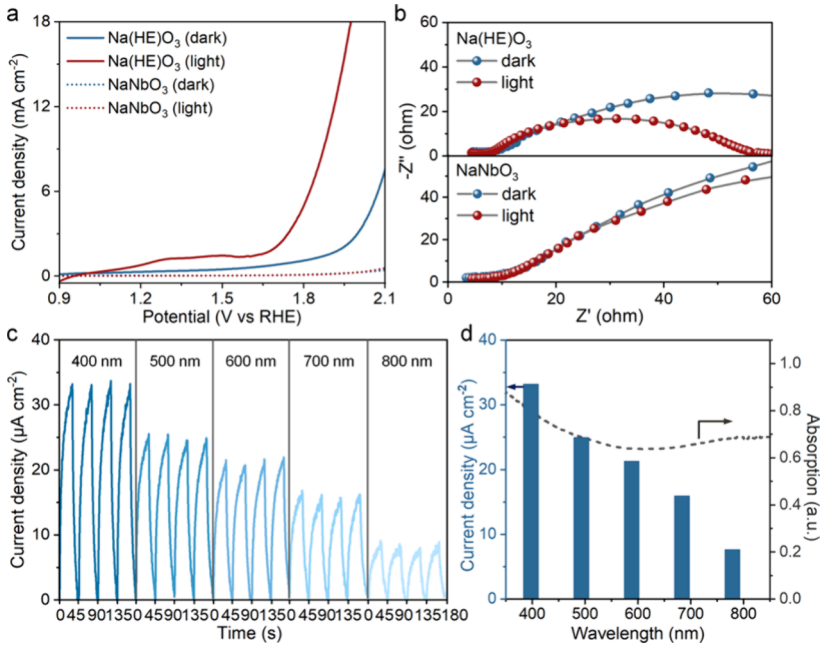

Figure 3. Photoelectrochemical characterization of $Na(HE)O_3$ photoanode measured in a standard three-electrode configuration. (a) LSV curves of $Na(HE)O_3$ and $NaNbO_3$ photoanodes recorded in dark and under visible light irradiation, respectively. (b) Nyquist plot of impedance spectra of $Na(HE)O_3$ and $NaNbO_3$ under dark and visible light conditions. (c) Photocurrent curves of $Na(HE)O_3$ under a series of monochromatic irradiation. (d) Dependence of the photocurrent density on the wavelength for $Na(HE)O_3$.

absorption spectroscopy (TAS) was performed under 365 and 800 nm excitations. As shown in Figure 2b and Figure S5, under 365 nm excitation, electrons are primarily excited from the valence band to the conduction band, producing an initial negative ΔA signal in the 420−600 nm region due to ground-state bleaching (τ_1 = 21.0 fs). Subsequently, this signal evolves into positive ΔA features (τ_2 = 312.3 ps, τ_3 = 403.3 ps), which are attributed to carrier relaxation and then captured into mid-gap states. Besides, under 800 nm excitation, electrons are directly excited from the intermediate band to the conduction band, leading to negative ΔA signals from 550 to 650 nm associated with depopulation of midgap states (Figures S6 and S7). These spectroscopic results support a two-step photo-excitation process in $Na(HE)O_3$ mediated by a broadened and partially filled mid-gap electronic manifold that resembles an intermediate band rather than discrete defect states.[52−55]

The involvement of an intermediate band in carrier dynamics is further supported by photoluminescence spectroscopy (PL). Shown in Figure 2d is the PL spectrum of $Na(HE)O_3$ excited under 325 nm excitation. The PL spectrum exhibits typical features of a wide-bandgap semiconductor, consisting of two distinct emission components.[56,57] A sharp emission peak at approximately 385 nm is assigned to near-band-edge recombination, whereas a broad emission band spanning the visible region is observed. This visible emission can be reasonably attributed to radiative recombination processes involving the intermediate band, indicating that photoexcited carriers associated with the delocalized intermediate band undergo scattering or diffusion toward multiple luminescence centers, thereby producing emission signals over a wide spectral range. In Figure 2e, time-resolved photoluminescence (TRPL) measurements were further conducted by using a 325 nm pulsed laser. The band-edge emission at 380 nm decays rapidly (1.98 ns), while emissions at 500 and 550 nm display prolonged lifetimes, reflecting the recombination process mediated by intermediate-band states.

In conventional perovskite oxides such as $NaNbO_3$ and $NaTaO_3$, the conduction band is mainly composed of metal d states, while the valence band is mostly contributed by O 2p states.[58] Due to a large difference in electronegativity between the transition-metal cations and the oxygen, these materials typically exhibit wide bandgaps and limited visible-light absorption. For $Na(HE)O_3$, X-ray photoelectron spectroscopy (XPS) analysis shows that Nb^{5+} and Ta^{5+} remain in their highest oxidation states with d^0 electronic configurations. Meanwhile, the other transition-metal cations, including V, Mo, W, Cr, Ru, Co, and Cu, display mixed-valence states, indicating the coexistence of both closed-shell d^0 and open-shell d^n cations (Figures S8 and S9). Such mixed oxidation states can be reasonably attributed to charge compensation effects within the high-entropy lattice. When aliovalent cations are incorporated into a shared lattice, the resulting local charge imbalance is compensated through the redistribution of electronic charges among neighboring cation sites. In addition, $Na(HE)O_3$ contains a relatively high concentration of oxygen vacancies, as verified by electron paramagnetic resonance (EPR), XPS, and STEM-ABF characterizations shown in Figures S10−S12, which can further contribute to local charge neutrality and promote electronic reconstruction within the lattice.

In this case, the conduction band of $Na(HE)O_3$ could still be derived by the d^0 metal centers, preserving the wide bandgap framework of the host lattice. Meanwhile, the incorporation of different open-shell cations introduces additional d states that interact with the O 2p orbitals. Because these multiple cations are randomly but homogeneously distributed over equivalent B-site positions, their electronic states tend to overlap and broaden rather than remain spatially localized, favoring the formation of a quasi-

https://doi.org/10.1021/jacs.6c02884
J. Am. Chem. Soc. 2026, 148, 25696−25706

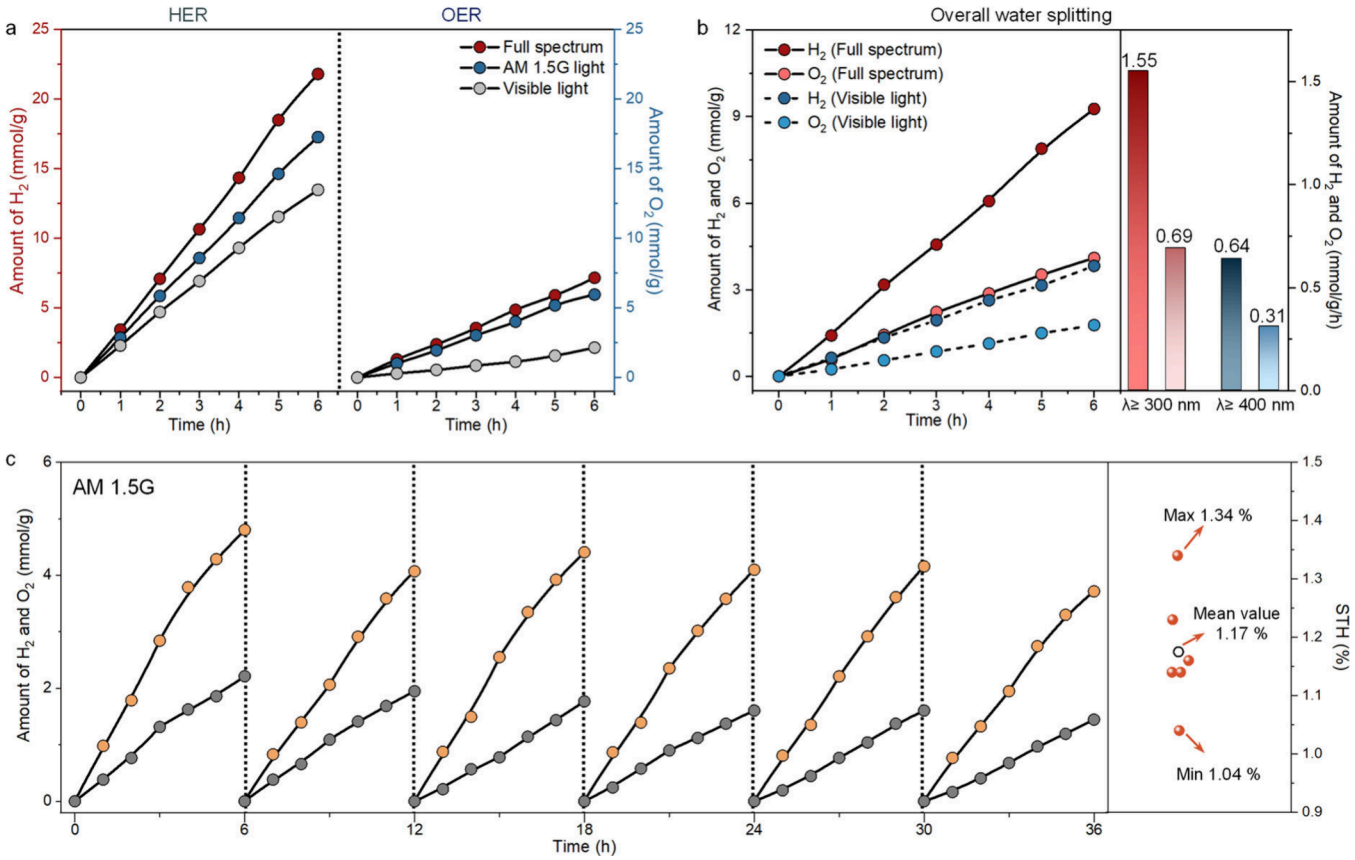

Figure 4. Photocatalytic performance of $Na(HE)O_3$ photocatalyst. (a) Photocatalytic hydrogen evolution reaction and oxygen evolution reaction rates over $Na(HE)O_3$ under different irradiation conditions. (b) Overall water-splitting performance showing simultaneous H_2 and O_2 production over $Na(HE)O_3$ under full-spectrum and visible-light irradiation. (c) Cycling stability of $Na(HE)O_3$ for photocatalytic overall water splitting under AM 1.5G simulated sunlight illumination. The reaction system was confirmed to be gastight by monitoring an invariant N_2 signal during the measurements. The right panel shows the STH efficiency calculated from the cycling results.

continuous intermediate band instead of discrete defect levels. It is further worth noting that, unlike the other constituent elements, Al does not possess d-orbital electrons, yet as reported in many high-entropy oxide systems, its incorporation helps stabilize the high-entropy lattice and further modulate the local electronic environment.[30,59] Raman spectroscopy provides complementary structural evidence (Figure 2f). The vibrational features are mainly associated with B-O bending and stretching modes.[60,61] Compared with $NaNbO_3$, the Raman spectra of $Na(HE)O_3$ show significant peak broadening without the appearance of new vibrational modes, indicating that chemical disorder at the B sites induces BO_6 octahedral distortions and relaxation of Raman selection rules while maintaining long-range lattice order.[62] Such a structure preserves the perovskite framework but introduces significant local symmetry breaking, which favors enhanced orbital hybridization and electronic state overlap.

Subsequently, Mott−Schottky (M-S) analysis and valence-band measurements were performed to evaluate the band structure of $Na(HE)O_3$. As shown in Figures 2g and S13, based on the M-S plot, the flat band of $Na(HE)O_3$ and pristine $NaNbO_3$ is estimated to be approximately −0.89 V and −0.97 V versus RHE, respectively. Figure 2h and Figure S14 show the obtained valence-band spectra of $Na(HE)O_3$ and pristine $NaNbO_3$. Relative to $NaNbO_3$, the valence band (VB) edge of $Na(HE)O_3$ shifts closer to the Fermi level. More importantly, a weak yet well-resolved spectral feature emerges close to the Fermi level, which is consistent with the existence of the intermediate band within the bandgap.[63,64] This observation is also consistent with the sub-bandgap optical response in the UV−vis spectra. Such intermediate band states can be attributed to the strong local chemical disorder and distorted crystal fields inherent in high-entropy oxides, where multimetal random occupation enhances d-orbital hybridization, leading to band broadening and partial overlap of originally discrete electronic states.[40,50,51]

Further electronic structure analysis combining UPS, UV−vis absorption, and M-S measurements indicates that $Na(HE)O_3$ possesses a bandgap of approximately 2.83 eV, while pristine $NaNbO_3$ exhibits a bandgap of approximately 3.29 eV (Figures 2i and S14). The intermediate band is further estimated to lie approximately 1.0−1.5 eV below the conduction band minimum. Taken together, $Na(HE)O_3$ maintains band-edge positions that straddle the redox potentials required for overall water splitting, while the intermediate band within the bandgap could facilitate stepwise photoexcitation processes, thereby enhancing broadband light absorption and improving charge-carrier utilization for photocatalysis.

Photoelectrochemical (PEC) measurements were conducted to investigate the charge separation behavior and photoresponse of $Na(HE)O_3$. Figure 3a shows the photocurrent density−potential (J−V) curves obtained by linear sweep voltammetry in the potential range of 0.9−2.1 V vs RHE for

https://doi.org/10.1021/jacs.6c02884
J. Am. Chem. Soc. 2026, 148, 25696−25706

$Na(HE)O_3$ and pristine $NaNbO_3$ photoanodes. Notably, the $Na(HE)O_3$ photoanode delivers a photocurrent density of 0.85 mA cm^{-2} at 1.23 V vs RHE under visible light irradiation, which is significantly higher than that of $NaNbO_3$, reflecting enhanced visible-light utilization. Electrochemical impedance spectroscopy (EIS) in Figure 3b reveals that $Na(HE)O_3$ exhibits a smaller Nyquist arc than $NaNbO_3$ in the dark, corresponding to a lower interfacial charge-transfer resistance. These impedance spectra were analyzed using an appropriate equivalent-circuit model (Figure S15 and Table S3). Upon visible-light illumination, the further decrease in impedance response of $Na(HE)O_3$ indicates the participation of photogenerated charge carriers in the interfacial process. In addition, it can be seen that $Na(HE)O_3$ photoanode rapidly generates a photocurrent under visible light illumination, showing a current density of 78.4 μA cm^{-2} at an applied potential of 0.4 V vs Ag/AgCl (Figure S16). Furthermore, $Na(HE)O_3$ also exhibits the photocurrent density under different monochromatic excitations in the visible and near-infrared regions (Figure 3c). In this situation, those low-energy photons are insufficient to directly excite valence band electrons to the conduction band, thereby indicating the involvement of sub-bandgap excitation pathways associated with the intermediate band. The broadband photocurrent response summarized in Figure 3d suggests its broadband photoactivity enabled by the inner-Z-scheme, allowing low-energy visible photons to be harvested efficiently to drive photocatalytic reactions.

Shown in Figure 4a are the photocatalytic activities for water splitting, including both the hydrogen evolution reaction (HER) and the oxygen evolution reaction (OER), under different illumination conditions. In a 20 vol % methanol aqueous solution, $Na(HE)O_3$ exhibits a hydrogen evolution rate of 3.61 mmol g^{-1} h^{-1} under full-spectrum irradiation. Notably, an appreciable H_2 evolution activity is observed under AM 1.5G simulated sunlight and visible light irradiation ($\lambda \geq$ 400 nm). For oxygen evolution reaction, $Na(HE)O_3$ photocatalyst also exhibits measurable photocatalytic activity in a 1 mM $AgNO_3$ aqueous solution under different light irradiation conditions. The overall water-splitting performance of $Na(HE)O_3$ was further evaluated in phosphate-buffered saline (PBS) solution without the addition of any other cocatalysts. As shown in Figure 4b, $Na(HE)O_3$ achieves H_2 and O_2 evolution rates of 1.55 and 0.69 mmol g^{-1} h^{-1} under full-spectrum irradiation, which remain high at 0.64 and 0.31 mmol g^{-1} h^{-1} under visible light irradiation. Moreover, it is noted that a slight deviation from the stoichiometric H_2/O_2 ratio of 2:1 was observed. Such deviations have been widely reported in photocatalytic systems and are generally attributed to competing surface redox processes.[65,66] As for the photocatalytic system of $Na(HE)O_3$, dissolved O_2 can be activated by photogenerated electrons to form reactive oxygen species, primarily including superoxide ($*O_2^-$) and hydroperoxyl (*OOH) intermediates, as evidenced by EPR and in situ ATR-FTIR measurements (Figures S17 and S18). Therefore, the oxygen reduction process may slightly decrease the measured O_2 evolution.

As illustrated in Figure 4c, cycling tests show no significant decay in either the H_2 or O_2 evolution rates, highlighting the structural stability of this high-entropy photocatalyst. Additionally, there were no significant changes in the XRD and Raman spectra of $Na(HE)O_3$ before and after the photocatalytic reaction (Figure S19). According to the photocatalytic performance under AM 1.5G simulated sunlight irradiation, the solar-to-hydrogen (STH) efficiency is estimated to be approximately 1.34% (Figure S20). As shown in Figure S21, the AQE under monochromatic light of an irradiation wavelength of 400 nm is up to 3.97%. The overall water-splitting performance of the $Na(HE)O_3$ photocatalyst arises from a delicate yet effective balance between band structure and chemical complexity.

The chemical complexity and lattice distortion inherent in high-entropy oxides give rise to a broad distribution of local coordination environments at the surface. This structural heterogeneity could enhance the catalytic functionality by generating a wide spectrum of adsorption energies for reaction intermediates. Such behavior has been extensively recognized in high-entropy catalytic systems, particularly for the hydrogen evolution reaction.[33,41,67] However, their application in photocatalytic oxygen evolution has been less extensively explored, owing to the higher thermodynamic barrier and the more complex multielectron transfer kinetics. To investigate the role of composition, we selectively removed certain open-shell cations to construct a series of high-entropy oxides with different elemental compositions (Ru_{none}-$Na(HE)O_3$, Cu_{none}-$Na(HE)O_3$, and Ru/Co/Cu_{none}-$Na(HE)O_3$). These samples retain the same crystal structure and morphology as $Na(HE)O_3$, and tSTEM-EDS mapping results confirm that the elemental distributions remain homogeneous after compositional modulation (Figures S22−S24). As shown in Figure 5a, the random removal of open-shell metal cations leads to a decline in the overall water-splitting activity, although the extent of performance loss varies slightly among different compositions. These results indicate that the catalytic activity of $Na(HE)O_3$ does not originate from any single metal center

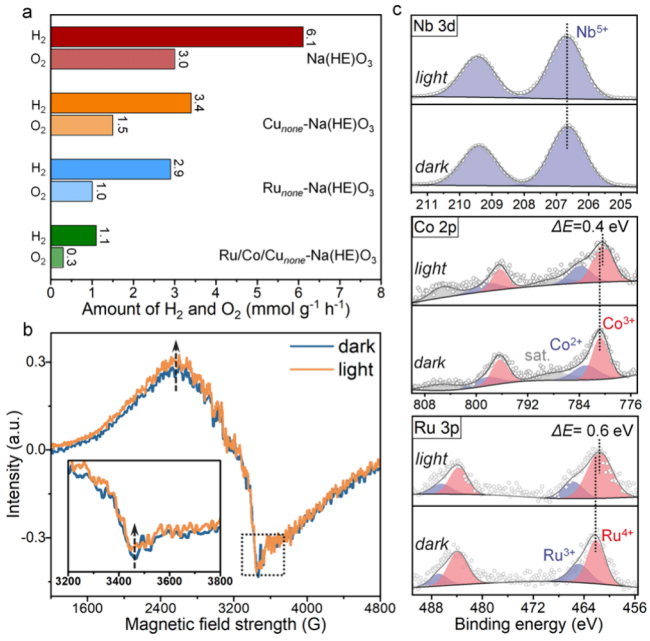

Figure 5. Composition effect and photoinduced electronic response of $Na(HE)O_3$. (a) H_2 and O_2 production rates for photocatalytic overall water splitting over the $Na(HE)O_3$, Cu_{none}-$Na(HE)O_3$, Ru_{none}-$Na(HE)O_3$, and Ru/Co/Cu_{none}-$Na(HE)O_3$, showing the influence of selectively removing open-shell cations. (b) EPR spectra of $Na(HE)O_3$ recorded in the dark and under visible-light irradiation. (c) XPS spectra of Nb 3d, Co 2p, and Ru 3p of $Na(HE)O_3$ recorded in the dark and under light irradiation.

https://doi.org/10.1021/jacs.6c02884
J. Am. Chem. Soc. 2026, 148, 25696−25706

but instead arises from the cooperative contributions of multiple cations. For open-shell metal species, characterized by partially filled d orbitals and electronic flexibility, they play a dominant role in modulating the local electronic structure at the surface and the associated variations in adsorption energies of reaction intermediates. Therefore, when multiple open-shell metal cations are simultaneously removed, the H_2 and O_2 evolution ratio shows the most substantial decline.

To further probe the electronic environment in $Na(HE)O_3$, EPR spectroscopy and XPS measurements under visible light illumination were performed. In the dark, the EPR spectrum displays a complex line shape composed of multiple paramagnetic contributions (Figure 5b). A broad asymmetric component is observed, which is characteristic of strong spin−spin interactions among exchange-coupled open-shell transition-metal centers distributed within the high-entropy lattice.[68,69] Meanwhile, local coordination distortions and chemical disorder further enhance exchange coupling and spin relaxation processes, collectively leading to pronounced line broadening. Upon visible light irradiation, a redistribution of EPR signal intensity occurs. The broad component increases, whereas the sharper component decreases slightly. While the precise assignment of the overlapping EPR features is intrinsically challenging in multication systems, this light-induced intensity redistribution suggests that photogenerated carriers have undergone a redistribution process due to the different local chemical environments. Complementary evidence for element-dependent carrier redistribution is provided by XPS measurements under visible light illumination. All binding energy shifts were calibrated against the C 1s reference. As shown in Figures 5c, S25, and S26, closed-shell cations such as Nb and Ta remain in their initial highest oxidation states, whereas other open-shell and mixed-valence species exhibit measurable binding energy shifts. For example, Ru and Co species exhibit a shift toward lower binding energy that indicates an increased higher oxidation state contribution under illumination.[70,71] Although the precise catalytic role of each metal species at B sites requires further clarification, the results suggest that different open-shell cations respond differently to photoexcitation, reflecting variations in local charge density. In $Na(HE)O_3$, efficient overall water splitting does not arise from certain active sites but instead emerges intrinsically from the high-entropy-stabilized coexistence of multiple cations within a single crystallographic lattice. These open-shell metal cations not only contribute to intermediate-band formation but also favor surface catalytic functionality.

CONCLUSION

We have designed and synthesized a high-entropy photocatalyst, $Na(HE)O_3$, that embodies the "inner-Z-scheme" electron transfer pathway within a single semiconductor. This "inner Z-scheme" architecture arises from entropy-enabled intermediate-band engineering in a wide-bandgap host through the selective incorporation of closed-shell and open-shell metal cations. The resulting intermediate band exhibits a quasi-continuous and partially filled character, which is fundamentally distinct from the isolated defect states typically introduced by conventional doping strategies in previous studies. Such a rationally designed electron transfer pathway supports stepwise two-photon excitation, allowing efficient harvesting of low-energy visible photons and therefore improved solar energy conversion and utilization. Meanwhile, the widely separated band edges defined by closed-shell d^0 metal cations maintain the well-separated conduction/valence band positions suitable for both hydrogen and oxygen evolution of overall water splitting. In addition, the open-shell d^n cations that are introduced for band engineering can also provide intrinsic catalytic sites on the photocatalyst surface for activating water redox reaction. Such photocatalysis activity enables visible-light-driven overall water splitting, thereby highlighting the particular promise of this high-entropy semiconductor photocatalyst for solar energy conversion and utilization.

This study offers fundamental insight into how the high degree of chemical complexity inherent in high-entropy materials can be harnessed for band-structure engineering of metal-oxide semiconductors toward solar energy conversion. The particular "inner-Z-scheme" design concept demonstrated here establishes a generalizable strategy for embedding the intermediate-band-enabled, stepwise photoexcitation functionality directly into a single semiconductor and thereby expands the design landscape of a new class of high-entropy photocatalysts for prospective applications.

ASSOCIATED CONTENT

Supporting Information

The Supporting Information is available free of charge at https://pubs.acs.org/doi/10.1021/jacs.6c02884.

Experimental details; additional SEM, HAADF-STEM, ABF-STEM, EDS mapping, XRD, Raman, EPR, FTIR results; Mott−Schottky curves; Rietveld refinement results, ICP-AES data, and catalytic measurements (PDF)

AUTHOR INFORMATION

Corresponding Authors

Muhua Sun − *Key Laboratory of Advanced Materials (MOE), School of Materials Science and Engineering, Tsinghua University, Beijing 100084, China*; Email: m_sun@tsinghua.edu.cn

Wenlong Wang − *Beijing National Laboratory for Condensed Matter Physics and Institute of Physics, Chinese Academy of Sciences, Beijing 100190, China; School of Physical Sciences, University of Chinese Academy of Sciences, Beijing 100190, China; Songshan Lake Materials Laboratory, Dongguan 523808, China*; orcid.org/0000-0003-4390-474X; Email: wwl@iphy.ac.cn

Authors

Hao Ling − *Beijing National Laboratory for Condensed Matter Physics and Institute of Physics, Chinese Academy of Sciences, Beijing 100190, China*

Aomiao Zhi − *Beijing National Laboratory for Condensed Matter Physics and Institute of Physics, Chinese Academy of Sciences, Beijing 100190, China*

Lei Liao − *Beijing National Laboratory for Condensed Matter Physics and Institute of Physics, Chinese Academy of Sciences, Beijing 100190, China; School of Physical Sciences, University of Chinese Academy of Sciences, Beijing 100190, China*

Yuanfang Feng − *Beijing National Laboratory for Condensed Matter Physics and Institute of Physics, Chinese Academy of Sciences, Beijing 100190, China; School of Physical Sciences, University of Chinese Academy of Sciences, Beijing 100190, China*

Yingying Lan − *Songshan Lake Materials Laboratory, Dongguan 523808, China*
Lejuan Cai − *Songshan Lake Materials Laboratory, Dongguan 523808, China;* orcid.org/0000-0002-1604-0344
Xudan Huang − *Beijing National Laboratory for Condensed Matter Physics and Institute of Physics, Chinese Academy of Sciences, Beijing 100190, China*
Lisha Lu − *Beijing National Laboratory for Condensed Matter Physics and Institute of Physics, Chinese Academy of Sciences, Beijing 100190, China; School of Physical Sciences, University of Chinese Academy of Sciences, Beijing 100190, China*
Renjie Li − *Songshan Lake Materials Laboratory, Dongguan 523808, China*
Qi Guo − *Zhejiang Metallurgical Research Institute Co., Ltd., Hangzhou 310000, China*
Meiyun Li − *Beijing National Laboratory for Condensed Matter Physics and Institute of Physics, Chinese Academy of Sciences, Beijing 100190, China; School of Physical Sciences, University of Chinese Academy of Sciences, Beijing 100190, China*
Jingkun Zhang − *State Key Laboratory of Mesoscience and Engineering, Institute of Process Engineering, Chinese Academy of Sciences, Beijing 100190, China*
Lifen Wang − *Beijing National Laboratory for Condensed Matter Physics and Institute of Physics, Chinese Academy of Sciences, Beijing 100190, China; School of Physical Sciences, University of Chinese Academy of Sciences, Beijing 100190, China;* orcid.org/0000-0002-8468-5048
Xuedong Bai − *Beijing National Laboratory for Condensed Matter Physics and Institute of Physics, Chinese Academy of Sciences, Beijing 100190, China; School of Physical Sciences, University of Chinese Academy of Sciences, Beijing 100190, China; Songshan Lake Materials Laboratory, Dongguan 523808, China;* orcid.org/0000-0002-1403-491X

Complete contact information is available at: https://pubs.acs.org/10.1021/jacs.6c02884

Author Contributions

All authors have given approval to the final version of the manuscript.

Notes

The authors declare no competing financial interest.

■ ACKNOWLEDGMENTS

This work was supported by the Guangdong Major Project of Basic and Applied Basic Research (2021B0301030002), the National Natural Science Foundation of China (12334001 and 52427802), the National Key Research and Development Program of China (2024YFA1208201), and the Open Research Fund of State Key Laboratory of Mesoscience and Engineering (MESO-25-D08).

■ REFERENCES

(1) Hisatomi, T.; Domen, K. Reaction systems for solar hydrogen production via water splitting with particulate semiconductor photocatalysts. *Nat. Catal.* **2019**, *2* (5), 387−399.
(2) Lewis, N. S. Research opportunities to advance solar energy utilization. *Science* **2016**, *351* (6271), 1920.
(3) Sun, K.; Huang, Y.; Sun, F.; Wang, Q.; Zhou, Y.; Wang, J.; Zhang, Q.; Zheng, X.; Fan, F.; Luo, Y.; et al. Dynamic structural twist in metal−organic frameworks enhances solar overall water splitting. *Nat. Chem.* **2024**, *16* (10), 1638−1646.
(4) Wang, Q.; Hisatomi, T.; Jia, Q.; Tokudome, H.; Zhong, M.; Wang, C.; Pan, Z.; Takata, T.; Nakabayashi, M.; Shibata, N.; et al. Scalable water splitting on particulate photocatalyst sheets with a solar-to-hydrogen energy conversion efficiency exceeding 1%. *Nat. Mater.* **2016**, *15* (6), 611−615.
(5) Navalón, S.; Dhakshinamoorthy, A.; Álvaro, M.; Ferrer, B.; García, H. Metal−Organic Frameworks as Photocatalysts for Solar-Driven Overall Water Splitting. *Chem. Rev.* **2023**, *123* (1), 445−490.
(6) Zhao, Z.; Goncalves, R. V.; Barman, S. K.; Willard, E. J.; Byle, E.; Perry, R.; Wu, Z.; Huda, M. N.; Moulé, A. J.; Osterloh, F. E. Electronic structure basis for enhanced overall water splitting photocatalysis with aluminum doped SrTiO3 in natural sunlight. *Energy Environ. Sci.* **2019**, *12* (4), 1385−1395.
(7) Nishioka, S.; Osterloh, F. E.; Wang, X.; Mallouk, T. E.; Maeda, K. Photocatalytic water splitting. *Nat. Rev. Methods Primers* **2023**, *3* (1), 42.
(8) Ogawa, K.; Suzuki, H.; Zhong, C.; Sakamoto, R.; Tomita, O.; Saeki, A.; Kageyama, H.; Abe, R. Layered Perovskite Oxyiodide with Narrow Band Gap and Long Lifetime Carriers for Water Splitting Photocatalysis. *J. Am. Chem. Soc.* **2021**, *143* (22), 8446−8453.
(9) Xiao, J.; Hisatomi, T.; Domen, K. Narrow-Band-Gap Particulate Photocatalysts for One-Step-Excitation Overall Water Splitting. *Acc. Chem. Res.* **2023**, *56* (7), 878−888.
(10) Yu, J.; Shi, L.; Li, R.; Huang, J.; Wang, R.; Li, Z.; Shen, C.; Liu, G.; Li, Y.; Xu, X. Single-Crystalline $LaTiO_2N$ Nanosheets with Regulated Defects for Photocatalytic Overall Water Splitting under Visible Light up to 600 nm. *ACS Catal.* **2024**, *14* (2), 608−618.
(11) Abdul Nasir, J.; Munir, A.; Ahmad, N.; Haq, T.u.; Khan, Z.; Rehman, Z. Photocatalytic Z-Scheme Overall Water Splitting: Recent Advances in Theory and Experiments. *Adv. Mater.* **2021**, *33* (52), No. 2105195.
(12) Lin, L.; Ma, Y.; Vequizo, J. J. M.; Nakabayashi, M.; Gu, C.; Tao, X.; Yoshida, H.; Pihosh, Y.; Nishina, Y.; Yamakata, A.; et al. Efficient and stable visible-light-driven Z-scheme overall water splitting using an oxysulfide H_2 evolution photocatalyst. *Nat. Commun.* **2024**, *15* (1), 397.
(13) Ma, Y.; Lin, L.; Takata, T.; Hisatomi, T.; Domen, K. A perspective on two pathways of photocatalytic water splitting and their practical application systems. *Phys. Chem. Chem. Phys.* **2023**, *25* (9), 6586−6601.
(14) Nagpal, P.; Klimov, V. I. Role of mid-gap states in charge transport and photoconductivity in semiconductor nanocrystal films. *Nat. Commun.* **2011**, *2* (1), 486.
(15) Wang, Z.; Luo, Y.; Hisatomi, T.; Vequizo, J. J. M.; Suzuki, S.; Chen, S.; Nakabayashi, M.; Lin, L.; Pan, Z.; Kariya, N.; et al. Sequential cocatalyst decoration on $BaTaO_2N$ towards highly-active Z-scheme water splitting. *Nat. Commun.* **2021**, *12* (1), 1005.
(16) Luque, A.; Martí, A. The Intermediate Band Solar Cell: Progress Toward the Realization of an Attractive Concept. *Adv. Mater.* **2010**, *22* (2), 160−174.
(17) Vijayan, K.; Thirumalaisamy, L.; Vijayachamundeeswari, S. P.; Sivaperuman, K.; Ahsan, N.; Okada, Y. A Novel Approach for Designing a Sub-Bandgap in $CuGa(S,Te)_2$ Thin Films Assisted with Numerical Simulation of Solar Cell Devices for Photovoltaic Application. *ACS Omega.* **2023**, *8* (25), 22414−22427.
(18) Xu, S.-H.; Zhou, D. Y.; Liao, L. S. Quantum-Dot Intermediate Band Semiconductors: From Materials to Applications. *Adv. Opt. Mater.* **2025**, *13* (32), No. e01521.
(19) Ding, Q.; Zhang, Y.; Chen, X.; Fu, X.; Chen, D.; Chen, S.; Gu, L.; Wei, F.; Bei, H.; Gao, Y.; et al. Tuning element distribution, structure and properties by composition in high-entropy alloys. *Nature* **2019**, *574* (7777), 223−227.
(20) Hsu, W. L.; Tsai, C.-W.; Yeh, A.-C.; Yeh, J.-W. Clarifying the four core effects of high-entropy materials. *Nat. Rev. Chem.* **2024**, *8* (6), 471−485.
(21) Yao, Z.; Chen, Y.; Wang, X.; Hu, K.; Ren, S.; Zhang, J.; Song, Z.; Ren, N.; Duan, X. High-entropy alloys catalyzing polymeric

transformation of water pollutants with remarkably improved electron utilization efficiency. *Nat. Commun.* **2025**, *16* (1), 148.
(22) Zeng, K.; Hu, R.; Zhang, J.; Li, X.; Xu, Y.; Mu, X.; Wu, H.; Liu, S.; Liu, H.; Chen, J.; et al. Finely tailoring the local ensembles in heterostructured high entropy alloy catalysts through pulsed annealing. *Nat. Commun.* **2025**, *16* (1), 3403.
(23) Zhang, M.; Gao, Y.; Xie, C.; Duan, X.; Lu, X.; Luo, K.; Ye, J.; Wang, X.; Gao, X.; Niu, Q.; et al. Designing water resistant high entropy oxide materials. *Nat. Commun.* **2024**, *15* (1), 8306.
(24) Li, M.; Lin, F.; Zhang, S.; Zhao, R.; Tao, L.; Li, L.; Li, J.; Zeng, L.; Luo, M.; Guo, S. High-entropy alloy electrocatalysts go to (sub-)nanoscale. *Sci. Adv.* **2024**, *10* (23), eadn2877.
(25) Sen, S.; Palabathuni, M.; Ryan, K. M.; Singh, S. High Entropy Oxides: Mapping the Landscape from Fundamentals to Future Vistas. *ACS Energy Lett.* **2024**, *9* (8), 3694−3718.
(26) Xu, W.; Diesen, E.; He, T.; Reuter, K.; Margraf, J. T. Discovering High Entropy Alloy Electrocatalysts in Vast Composition Spaces with Multiobjective Optimization. *J. Am. Chem. Soc.* **2024**, *146* (11), 7698−7707.
(27) Batchelor, T. A. A.; Pedersen, J. K.; Winther, S. H.; Castelli, I. E.; Jacobsen, K. W.; Rossmeisl, J. High-Entropy Alloys as a Discovery Platform for Electrocatalysis. *Joule* **2019**, *3* (3), 834−845.
(28) Wang, Y.; Mi, J.; Wu, Z. S. Recent status and challenging perspective of high entropy oxides for chemical catalysis. *Chem. Catal.* **2022**, *2* (7), 1624−1656.
(29) Gross, M. A.; Reynal, A.; Durrant, J. R.; Reisner, E. Versatile Photocatalytic Systems for H_2 Generation in Water Based on an Efficient DuBois-Type Nickel Catalyst. *J. Am. Chem. Soc.* **2014**, *136* (1), 356−366.
(30) Tsubota, H.; Jitianu, A.; Kawamura, G. Recent Advances in High-Entropy Oxides for Photocatalytic Applications. *ACS Mater. Lett.* **2025**, *7* (3), 1042−1056.
(31) Zou, J.; Tang, L.; He, W.; Zhang, X. High-Entropy Oxides: Pioneering the Future of Multifunctional Materials. *ACS Nano* **2024**, *18* (51), 34492−34530.
(32) Das, S.; Kumar, S.; Sarkar, S.; Pradhan, D.; Tiwary, C. S.; Chowdhury, S. High entropy spinel oxide nanoparticles for visible light-assisted photocatalytic degradation of binary mixture of antibiotic pollutants in different water matrixes. *J. Mater. Chem. A* **2024**, *12* (27), 16815−16830.
(33) Edalati, P.; Shen, X. F.; Watanabe, M.; Ishihara, T.; Arita, M.; Fuji, M.; Edalati, K. High-entropy oxynitride as a low-bandgap and stable photocatalyst for hydrogen production. *J. Mater. Chem. A* **2021**, *9* (26), 15076−15086.
(34) Katzbaer, R. R.; dos Santos Vieira, F. M.; Dabo, I.; Mao, Z.; Schaak, R. E. Band Gap Narrowing in a High-Entropy Spinel Oxide Semiconductor for Enhanced Oxygen Evolution Catalysis. *J. Am. Chem. Soc.* **2023**, *145* (12), 6753−6761.
(35) Siniard, K.; Fan, J.; Li, M.; Wang, Q.; Ivanov, A. S.; Wang, T.; Dai, S. A General Strategy for Bandgap Engineering Via Anion-Lattice Doping in High-Entropy Oxides. *Adv. Sci.* **2025**, *12* (34), No. 05789.
(36) Rahaman, M. Z.; Akther Hossain, A. K. M. Effect of metal doping on the visible light absorption, electronic structure and mechanical properties of non-toxic metal halide $CsGeCl_3$. *RSC Adv.* **2018**, *8* (58), 33010−33018.
(37) Tsuchikado, H.; Anabuki, S.; Cretu, O.; Kinoshita, Y.; Hattori, M.; Shiroma, Y.; Fan, D.; Okazaki, M.; Soma, T.; Ishiwari, F.; et al. Effects of Metal-Cation Doping on Photocatalytic H_2 Evolution Activity of Layered Perovskite Oxynitride $K_2LaTa_2O_6N$. *ACS Appl. Energy Mater.* **2025**, *8* (6), 3541−3552.
(38) Xiao, Y.; Fan, Z.; Nakabayashi, M.; Li, Q.; Zhou, L.; Wang, Q.; Li, C.; Shibata, N.; Domen, K.; Li, Y. Decoupling light absorption and carrier transport via heterogeneous doping in Ta_3N_5 thin film photoanode. *Nat. Commun.* **2022**, *13* (1), 7769.
(39) Zhang, N.; Chen, D.; Niu, F.; Wang, S.; Qin, L.; Huang, Y. Enhanced visible light photocatalytic activity of Gd-doped $BiFeO_3$ nanoparticles and mechanism insight. *Sci. Rep.* **2016**, *6* (1), No. 26467.
(40) Li, K.; Sun, L.; Bai, W.; Ma, N.; Zhao, C.; Zhao, J.; Xiao, C.; Xie, Y. High-Entropy Strategy to Achieve Electronic Band Convergence for High-Performance Thermoelectrics. *J. Am. Chem. Soc.* **2024**, *146* (20), 14318−14327.
(41) Ling, H.; Sun, M.; Han, H.; Lu, L.; Cai, L.; Lan, Y.; Li, R.; Chen, P.; Tian, X.; Bai, X.; et al. High-Entropy Lithium Niobate Nanocubes for Photocatalytic Water Splitting under Visible Light. *J. Phys. Chem. Lett.* **2024**, *15* (19), 5103−5111.
(42) Ling, H.; Sun, H.; Lu, L.; et al. Sustainable photocatalytic hydrogen peroxide production over octonary high-entropy oxide. *Nat. Commun.* **2024**, *15*, 9505.
(43) Kastuar, S. M.; Ekuma, C. E. Chemically tuned intermediate band states in atomically thin CuxGeSe/SnS quantum material for photovoltaic applications. *Sci. Adv.* **2024**, *10* (15), No. eadl6752.
(44) Lun, Z.; Ouyang, B.; Kwon, D.-H.; Ha, Y.; Foley, E. E.; Huang, T.-Y.; Cai, Z.; Kim, H.; Balasubramanian, M.; Sun, Y.; et al. Cation-disordered rocksalt-type high-entropy cathodes for Li-ion batteries. *Nat. Mater.* **2021**, *20* (2), 214−221.
(45) Lonergan, J.; Goncharov, V.; Swinhart, M.; Makovsky, K.; Rollog, M.; McNamara, B.; Clark, R.; Cutforth, D.; Armstrong, C.; Guo, X. F.; Paviet, P. Thermodynamic investigation of the NaCl-KCl salt system from 25 to 950 °C. *J. Mol. Liq.* **2023**, *391*, 122591.
(46) Aamlid, S. S.; Oudah, M.; Rottler, J.; Hallas, A. M. Understanding the Role of Entropy in High Entropy Oxides. *J. Am. Chem. Soc.* **2023**, *145* (11), 5991−6006.
(47) Rost, C. M.; Sachet, E.; Borman, T.; Moballegh, A.; Dickey, E. C.; Hou, D.; Jones, J. L.; Curtarolo, S.; Maria, J. P. Entropy-stabilized oxides. *Nat. Commun.* **2015**, *6*, 8485.
(48) Su, L.; Huyan, H.; Sarkar, A.; Gao, W.; Yan, X.; Addiego, C.; Kruk, R.; Hahn, H.; Pan, X. Direct observation of elemental fluctuation and oxygen octahedral distortion-dependent charge distribution in high entropy oxides. *Nat. Commun.* **2022**, *13* (1), 2358.
(49) Yao, S.; Yang, Z.; Yan, Y.-M.; Lin, Z. Multiscale electronic structure engineering of transition metal oxides: From atomic-scale, mesoscale, and external-field manipulation to multifunctional applications. *Prog. Mater. Sci.* **2026**, *158*, No. 101640.
(50) Katzbaer, R. R.; Dos Santos Vieira, F. M.; Dabo, I.; Mao, Z.; Schaak, R. E. Band Gap Narrowing in a High-Entropy Spinel Oxide Semiconductor for Enhanced Oxygen Evolution Catalysis. *J. Am. Chem. Soc.* **2023**, *145* (12), 6753−6761.
(51) Qi, S.; Lei, Z.; Huo, Q.; Zhao, J.; Huang, T.; Meng, N.; Liao, J.; Yi, J.; Shang, C.; Zhang, X.; et al. Ultrathin High-Entropy Fe-Based Spinel Oxide Nanosheets with Metalloid Band Structures for Efficient Nitrate Reduction toward Ammonia. *Adv. Mater.* **2024**, *36* (27), No. e2403958.
(52) Yang, C.; Qin, M.; Wang, Y.; Wan, D.; Huang, F.; Lin, J. Observation of an Intermediate Band in Sn-doped Chalcopyrites with Wide-spectrum Solar Response. *Sci. Rep.* **2013**, *3* (1), 1286.
(53) Luque, A.; Martí, A.; Stanley, C. Understanding intermediate-band solar cells. *Nat. Photonics.* **2012**, *6* (3), 146−152.
(54) Liu, Q.; Cai, Z.; Han, D.; Chen, S. Natural Intermediate Band in I 2 -II-IV-VI4 Quaternary Chalcogenide Semiconductors. *Sci. Rep.* **2018**, *8* (1), 1604.
(55) Selim, S.; Pastor, E.; García-Tecedor, M.; Morris, M. R.; Francàs, L.; Sachs, M.; Moss, B.; Corby, S.; Mesa, C. A.; Gimenez, S.; et al. Impact of Oxygen Vacancy Occupancy on Charge Carrier Dynamics in BiVO4 Photoanodes. *J. Am. Chem. Soc.* **2019**, *141* (47), 18791−18798.
(56) Wang, W.; Lin, A. S.; Phillips, J. D.; Metzger, W. K. Generation and recombination rates at ZnTe:O intermediate band states. *Appl. Phys. Lett.* **2009**, *95* (26), No. 261107.
(57) Welna, M.; Baranowski, M.; Linhart, W. M.; Kudrawiec, R.; Yu, K. M.; Mayer, M.; Walukiewicz, W. Multicolor emission from intermediate band semiconductor ZnO1−xSex. *Sci. Rep.* **2017**, *7* (1), No. 44214.
(58) Varignon, J.; Bibes, M.; Zunger, A. Origin of band gaps in 3d perovskite oxides. *Nat. Commun.* **2019**, *10* (1), 1658.
(59) Guo, M.; Liu, Y.; Zhang, F.; Cheng, F.; Cheng, C.; Miao, Y.; Gao, F.; Yu, J. Inactive Al^{3+}-doped $La(CoCrFeMnNiAlx)_{1/(5+x)}O_3$

https://doi.org/10.1021/jacs.6c02884
J. Am. Chem. Soc. 2026, 148, 25696−25706

high-entropy perovskite oxides as high performance supercapacitor electrodes. *J. Adv. Ceram.* **2022**, *11* (5), 742−753.
(60) Cui, H.; Huang, X. X.; Jiang, X. L.; Zhu, C. M.; Wang, L. G.; Wang, R.; Lu, S.; Yu, G. B. In situ Raman scattering investigation of field-induced phase transition behavior in $Na_{1+x}NbO_3$ ceramics via nonstoichiometric regulation. *J. Appl. Phys.* **2025**, *137* (19), 194101.
(61) Sharma, A.; Bhardwaj, U.; Jain, D.; Kushwaha, H. S. $NaNbO_3$ Nanorods: Photopiezocatalysts for Elevated Bacterial Disinfection and Wastewater Treatment. *ACS Omega.* **2022**, *7* (9), 7595−7605.
(62) Tuschel, D. Effect of Dopants or Impurities on the Raman Spectrum of the Host Crystal. *Spectroscopy* **2017**, *32* (12), 13.
(63) Pan, S.; Liu, X.; Guo, M.; Yu, S.f.; Huang, H.; Fan, H.; Li, G. Engineering the intermediate band states in amorphous Ti3+-doped TiO2 for hybrid dye-sensitized solar cell applications. *J. Mater. Chem. A* **2015**, *3* (21), 11437−11443.
(64) Chen, F.; Liu, H.; Ji, Q.; Hu, L.; Ju, M.-G.; Cheng, F.; Wu, X.-J. Enhancing Near-Infrared Absorption by Modulation the Intermediate Band of Cu−Fe−S Semiconductors for Boosting Photocatalytic Hydrogenation of Nitroarenes. *Chem. Mater.* **2025**, *37* (9), 3113−3124.
(65) Chen, K.; Xiao, J.; Vequizo, J. J. M.; Hisatomi, T.; Ma, Y.; Nakabayashi, M.; Takata, T.; Yamakata, A.; Shibata, N.; Domen, K. Overall Water Splitting by a $SrTaO_2N$-Based Photocatalyst Decorated with an Ir-Promoted Ru-Based Cocatalyst. *J. Am. Chem. Soc.* **2023**, *145* (7), 3839−3843.
(66) Lin, L.; Ma, Y.; Vequizo, J. J. M.; Nakabayashi, M.; Gu, C.; Tao, X.; Yoshida, H.; Pihosh, Y.; Nishina, Y.; Yamakata, A.; et al. Efficient and stable visible-light-driven Z-scheme overall water splitting using an oxysulfide H_2 evolution photocatalyst. *Nat. Commun.* **2024**, *15* (1), 397.
(67) Edalati, P.; Wang, Q.; Razavi-Khosroshahi, H.; Fuji, M.; Ishihara, T.; Edalati, K. Photocatalytic hydrogen evolution on a high-entropy oxide. *J. Mater. Chem. A* **2020**, *8* (7), 3814−3821.
(68) Abdel-Mageed, A. M.; Wiese, K.; Hauble, A.; Bansmann, J.; Rabeah, J.; Parlinska-Wojtan, M.; Brückner, A.; Behm, R. J. Steering the selectivity in CO_2 reduction on highly active Ru/TiO_2 catalysts: Support particle size effects. *J. Catal.* **2021**, *401*, 160−173.
(69) Kobeleva, E.; Shabratova, E.; Azoulay, A.; MacQueen, R. W.; Karjule, N.; Shalom, M.; Lips, K.; McPeak, J. E. Long-Term Characterization of Oxidation Processes in Graphitic Carbon Nitride Photocatalyst Materials via Electron Paramagnetic Resonance Spectroscopy. *Molecules* **2023**, *28*, 6475.
(70) Gong, D.; Zeng, G. Low-temperature combustion of methane over graphene templated Co_3O_4 defective-nanoplates. *Sci. Rep.* **2021**, *11*, 12604.
(71) Qian, G.; Chen, J.; Yu, T.; Luo, L.; Yin, S. N-Doped Graphene-Decorated NiCo Alloy Coupled with Mesoporous NiCoMoO Nanosheet Heterojunction for Enhanced Water Electrolysis Activity at High Current Density. *Nano-Micro Lett.* **2021**, *13* (1), 77.

https://doi.org/10.1021/jacs.6c02884
J. Am. Chem. Soc. 2026, 148, 25696−25706